Pore-scale characterisation and modelling of CO$_2$ flow in tight sandstones using X-ray micro-CT; Knorringfjellet Formation of the Longyearbyen CO$_2$ Lab, Svalbard

Jeroen Van Stappen, Tim De Kock, Marijn A. Boone, Snorre Olaussen & Veerle Cnudde

Rocks of the Knorringfjellet Formation in Central Spitsbergen form a potential storage reservoir for CO$_2$ below Longyearbyen. They are characterised by a moderate porosity and low permeability. However, water injection tests have shown positive results and fractures are considered to facilitate fluid flow. Therefore, hard data on fracture parameters and pore characteristics should be analysed to better understand flow characteristics. Consequently, sandstone and conglomerate samples from the Knorringfjellet Formation were sampled and characterised with High Resolution X-ray Computed Tomography (HRXCT) at the Centre for X-ray Tomography at Ghent University, Belgium (UGCT). The dataset includes samples taken from drillholes in the vicinity of Longyearbyen drilled during the pilot phase of the Longyearbyen CO$_2$ project, as well as from the Knorringfjellet Formation outcrops at Konusdalen and Criocerasdalen. This was done in order to compare micro-fracture and pore parameters in both settings. With HRXCT, the samples were analysed at pore scale and quantitative information of the pore network and fractures was extracted. Pore networks were used for the modelling of CO$_2$ flow in specific samples and information on fracture aperture was obtained at a micrometre scale. The acquired dataset can be directly used for a better understanding of flow in the aquifer.

Jeroen Van Stappen, Department of Geology and Soil Science – UGCT, Ghent University, Krijgslaan 281 (S8), B–9000 Ghent, Belgium. Tim De Kock, Department of Geology and Soil Science – UGCT, Ghent University, Krijgslaan 281 (S8), B–9000 Ghent, Belgium. Marijn A. Boone, Department of Geology and Soil Science – UGCT, Ghent University, Krijgslaan 281 (S8), B–9000 Ghent, Belgium. Unit Sustainable Materials Management, VITO, B–2400, Mol, Belgium. Snorre Olaussen, Longyearbyen CO$_2$ Lab, University Centre in Svalbard, PB 156, 9171 Longyearbyen, Svalbard, Norway. Veerle Cnudde, Department of Geology and Soil Science – UGCT, Ghent University, Krijgslaan 281 (S8), B–9000 Ghent, Belgium.

E-mail corresponding author (Jeroen Van Stappen): jeroen.vanstappen@ugent.be

Published December 24. 2014.

Introduction

During the pilot phase (2007–2013) of the Longyearbyen CO$_2$ Lab project altogether eight drillholes were produced in the close vicinity of the city in order to identify potential reservoirs for storage of CO$_2$. Four of these drillholes reached the Triassic – Jurassic rocks of the Kapp Toscana Group at depths of approximately 700 m (Drillholes 2, 4, 5 and 7). The upper parts of the targeted reservoir succession are formed by the Knorringfjellet Formation, which forms an aquifer with potential for CO$_2$ entrapment. Knorringfjellet Formation rocks are also found in outcrops approximately 15 km northeast from Longyearbyen in, among others, the valleys Konusdalen and Criocerasdalen (Fig. 1). They are characterised by a moderate porosity and low permeability (<2 mD) (Braathen et al., 2012). In such low-permeable rocks, fractures are considered to be the primary pathways for fluid flow (Berkowitz, 2002; Ogata et al., 2012). Therefore, the rocks need to be characterised

in detail concerning the pore network and fractures found within them. Both in the field and in the available cores, samples are taken in order to compare these parameters in the two settings.

The Knorringfjellet Formation, which makes up the whole Wilhelmøya Subgroup in western, central and eastern Spitsbergen, is a condensed section of texturally mature sandstones, deposited on coastal plains and in deltaic to shallow-marine environments. It is recognised by the appearance of sandy phosphate conglomerates at the base (Slottet Bed) and in the upper part (Brentskardhaugen Bed). During the latest Cenozoic, after subsidence in a foreland basin system, almost 3 km of overburden rock was eroded (Throndsen, 1982). Because of the deep burial of these rocks, they experienced mechanical compaction resulting in dense grain packing and extensive quartz cementation (Mørk, 2013). This gives rise to low matrix permeabilities, which typically do not exceed 2 mD, and porosity values varying from 8 to 18 vol.% (Farokhpoor
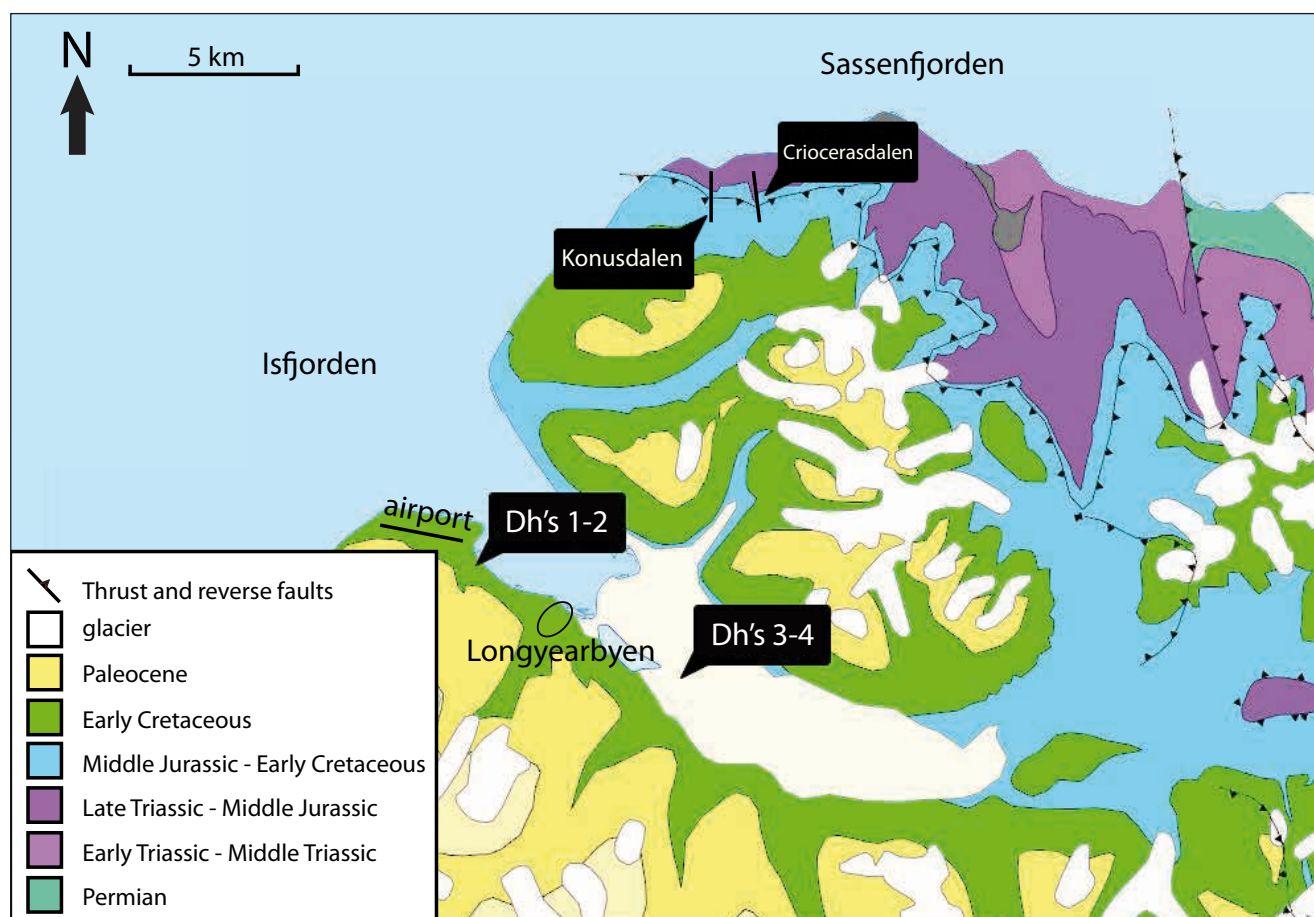
Figure 1. *Geological setting of the Longyearbyen (Svalbard) area, showing the locations of the sampling sites Dh2, Dh4 and the valleys Konusdalen and Criocerasdalen.*

et al., 2010, 2011). The target reservoir, however, was subjected to water injection tests after a primary observation of considerable loss of drilling fluid during the drilling of well Dh4. These tests indicate the presence of a localised high-permeability zone at a depth of circa 700 m in the Knorringfjellet Formation. The water injection tests confirmed the good injection potential of the reservoir (Braathen et al., 2012), utilising the natural fractures within the rocks (Braathen et al., 2012; Ogata et al., 2012). Therefore, rock fractures were studied in both drillcores and outcrops of the rock succession (Wærum, 2011; Ogata et al., 2012, 2014). They were characterised according to the frequency in which they occur and their orientation in the field at a mesoscopic scale. However, orientation of fractures in drillcores was impossible to determine, whereas televiewer data offered only limited orientational information. Also fracture apertures and lengths of individual fractures observed in cores were difficult to determine since they are only represented in two-dimensional (2D) cross sections through the rock succession. Together with the interconnectivity of fractures, these are important fracture parameters with regard to fluid flow. With high-resolution X-ray Computed Tomography (HRXCT) (Cnudde & Boone, 2013), however, information can be obtained on the internal structure of an investigated object in a non-destructive way. This technique reconstructs the object,

a rock sample, in three dimensions (3D), based on a set of two-dimensional (2D) projections, and thus poses a solution for detailed 3D analysis of rocks and the determination of parameters linked to pore space and micro-fractures. HRXCT was therefore the most promising method for characterising pore networks and especially fractures in samples of the Knorringfjellet Formation. Since macro- and mesoscopic properties of rocks are determined by their microstructure, their exact characterisation is of great importance for fluid flow. Specifically, the fracture parameters were a great source of uncertainty in the reservoir flow simulations carried out in the Longyearbyen CO_2 Lab project (Ogata et al., 2012, 2014).

Since 3D images of rock samples, obtained by HRXCT, can be used as a basis for rock modelling (Riepe et al., 2011), samples were selected for pore modelling and fluid-flow simulations. For these simulations, scans which obtained the highest resolutions (4 and 2.8 µm) were chosen. In this step, the pore network of a rock sample is simplified in order to conduct multi-phase fluid-flow simulations on it. This provides information on the trapping potential of non-wetting fluid phases, in this case liquid CO_2. Also, individual pores can be characterised quantitatively and fluid-flow properties can be determined (Bakke & Øren, 1997).

Materials

Mesoscopically, the rocks from the Knorringfjellet Formation of both wells Dh2 and Dh4 were described in detail. In Dh2, this unit is found at a depth from 733 to 755 m, and in Dh4 from 672 to 696 m. In these sections, facies changes were described as accurately as possible, levels of bioturbation and siderite were noted as well as pyrite nodules and fractures. The Knorringfjellet Formation starts in both Dh2 and Dh4 with a thin conglomerate bed, followed by a coarsening upwards sequence of homogeneous sandstones. This is the Slottet Bed; a unit which is regionally persistent (Mørk et al., 1999; Nagy & Berge, 2008) and is found in outcrop as a condensed sideritic pebbly sandstone unit which is bioturbated. Following the Slottet Bed is a succession of alternating sandstones and siltstones. Up-section, the frequency of siltstones increases, up to the start of the Brentskardhaugen Bed. The Brentskardhaugen Bed consists of conglomerates and coarse sandstones with characteristic ooids and phosphatic nodules; it is rich in glauconite and coal fragments in well Dh2 and contains a mixture of polymictic gravel with phosphate pebbles in well Dh4 (Bäckström & Nagy, 1985; Braathen et al., 2012). For the work presented here, sampling was primarily carried out in sandstone and conglomerate sections. This led to nine samples in Dh4 (C-samples) and three additional samples in Dh2 (D-samples). In Dh4, one conglomerate sample was selected (C7), one siltstone sample (C5), six sandstone samples (C1 to C4, C6 and C8) and one claystone sample (C9) which is part of the cap rock sequence (Jurassic Agardhfjellet Formation) overlying the Knorringfjellet Formation. In Dh2, two sandstone samples were collected (D1 and D3) and one siltstone sample in which vertical veins are found (D2). These samples were complemented with 10 individual field samples, taken in Konusdalen and Criocerasdalen (S- and T-samples), from which two conglomerate samples (S6 and S7) and 8 sandstone samples (T1 to T5, S2, S3 and S8) were analysed. In these valleys, a succession approximately 20 m thick was described with special attention paid to bioturbation, bedding of the rocks, fossil content and grain size. In order to compare results of the samples taken in the field with those taken from cores Dh2 and Dh4, three logs (Fig. 2) were constructed which can be correlated. The locations of the samples are given in each log (Fig. 2). In outcrop, the rocks of the Knorringfjellet Formation are partially covered by Quaternary deposits. These covered parts are approximately 3 to 5 m thick and are represented by gaps in the log in Fig. 2A.

Methods

Porosity and permeability in laboratory

Analysis of open porosity and permeability were carried out in laboratories at Ghent University (Belgium) and at the company PanTerra Geoconsultants B.V., respectively. To determine the open porosity of the samples, the standardised characterisation test for building stones was applied (NBN EN 1936:2006), using the Archimedes method with water saturation at vacuum conditions. PanTerra Geoconsultants B.V. additionally determined Helium-porosity on four core samples (C1, C3, C7 and C8). On the same samples, permeability measurements were carried out. The samples were chosen on the basis of their sedimentary facies, size, homogeneity and their correlation with the samples for which permeability measurements were carried out during the first phase of the CO_2 project (Braathen et al., 2010). To determine the permeability, steady-state gas permeability measurements were carried out. In this technique, air is forced through the sample at various pressures. For this research, the pressure was found in the range of 1 atm to approximately 4 atm, allowing measurement of the gas flow rate through the sample. Via Darcy's law, the permeability of the sample could then be calculated. Further analysis of the pore-size distributions was carried out on four subsamples (C4, C6, C7 and D3) with Mercury Intrusion Porosimetry (MIP) at the Magnel laboratory for Concrete Research, Ghent University. This technique, based on the capillary law, allows mercury penetration in nanopores and gives experimental values of average pore diameters and porosity distribution (León, 1998). A comparison of both techniques (water saturation porosimetry and MIP) is made in Cnudde et al. (2009), in which both techniques are elaborated upon and compared to micro-CT analysis.

The results from both the open porosity measurements and the permeability measurements were then compared to the results as published in the summary of the first phase of the CO_2 Project by Braathen et al. (2010, 2012).

CT-analysis

At the Centre for X-ray Tomography of Ghent University (UGCT; www.ugct.ugent.be), intensive research is carried out on the improvement of both hardware and software for HRXCT. The scanners are fully constructed by UGCT, as well as the data acquisition and reconstruction software packages (Vlassenbroeck et al., 2007; Brabant et al., 2011). Rock samples are placed on a rotating stage in between an X-ray point source and a detector as illustrated in Fig. 3. Due to the cone beam of the X-ray source, the resolution of the scanned images will be higher when a sample is placed close to the source. As a consequence, small samples can be scanned with a higher resolution in comparison with large samples. This is why samples are first scanned at a low resolution in order to obtain a general overview of the internal structures of the rocks, after which subsamples are scanned at higher resolution. Field samples were characterised with a diameter of 34 mm, while core samples had a diameter of 47 to 41 mm. These sizes led to primary resolutions of 41 μm and 56.6 to 62.6 μm, respectively. Based on these
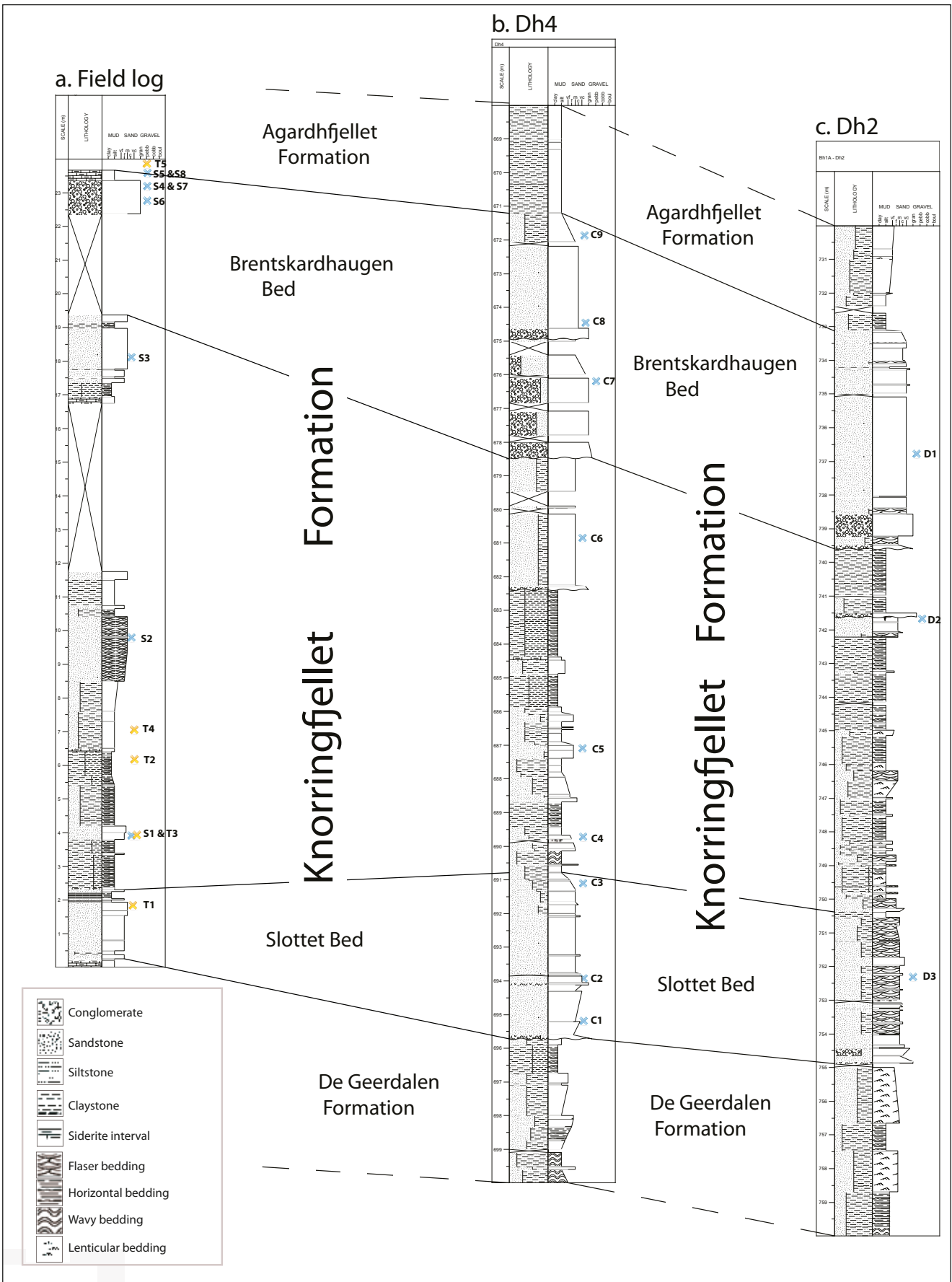
Figure 2. *Logs resulting from the fieldwork and drillcore studies. (A) represents the log of the combined fieldwork at Konusdalen and Criocerasdalen; (B) represents the log of Dh4 from 668 m to 700 m depth; (C) represents the same succession from a log of Dh2 from 730 m to 760 m depth.*
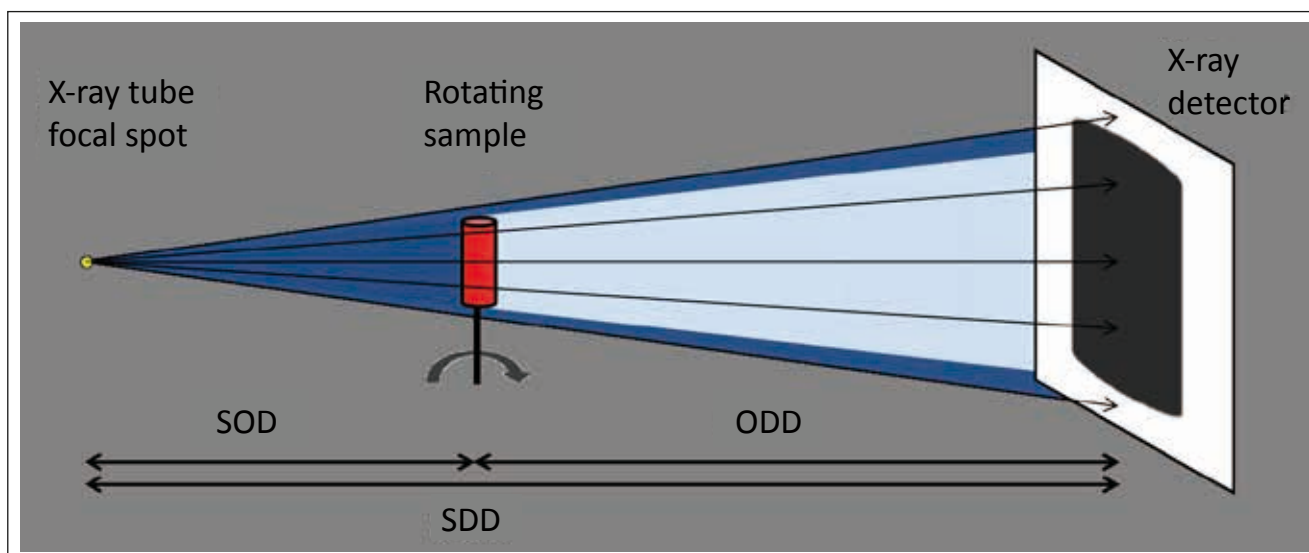
Figure 3. *Sketch of the setup of a scan using a cone beam configuration. The sample is mounted on a rotating stage between an X-ray source and an X-ray detector. Depending on the size of the sample, it can be moved closer to the source, resulting in a higher resolution. SOD: Source-Object Distance; ODD: Object-Detector-Distance; SDD: Source-Detector Distance. Figure from Cnudde & Boone (2013).*

scans, areas for subsampling were selected, which were taken with drill bits with internal diameters of 6 and 2 mm. For these subsamples, resolutions up to 2.8 µm were acquired. In Table 1, the scanning parameters are listed which were used for the different scans. All scans at low resolution, except for those of the Dh2 samples, were taken with a directional open-type Feinfocus tube. For higher resolutions, and for the Dh2 samples, the Feinfocus transmission head was used, which allows a smaller sample distance to the source and thus a smaller feature recognition (Masschaele et al., 2007). In all scans, the detector was a Varian 2520 V Paxscan panel. This detector consists of 2000 x 1600 pixels, with a pixel size of 127 µm. Other parameters, such as the number of radiographies, the hardware filter for beam hardening, the voltage, current and the exposure time were chosen according to the specific samples and the intended resolution.

After acquisition of the data, specialised software 'Octopus', developed by the UGCT, was used to reconstruct the 2D projections into a 3D image (Vlassenbroeck et al., 2007). The subsequent 3D analysis was carried out entirely in 'Morpho+' (Vlassenbroeck et al., 2007; Brabant et al., 2011). However, for the analysis of fractures a Multiscale Hessian Fracture Filtering (MSHFF) script had to be used in the program 'Fiji'. This script, developed by Voorn et al. (2013), allows segmentation of narrow fractures in 3D image data. After this, they are exported back to Morpho+ to extract quantitative information. Their opening (or aperture), defined as the diameter of the maximum inscribed sphere fitting inside the fracture, and length could then be determined. To determine the aperture distribution in individual fractures, the fracture is first divided in different objects after which the maximum opening

Table 1. *Summary of the scanning parameters at low (41.0 to 62.6 µm) and high resolutions (2.8 to 4 µm).*

Sample Series	X-ray tube	X-ray detector	# radio-graphies	Filter	Voltage (V)	Current (A)	exp. time (ms)	total scan time (min)
Low resolution								
Field samples S	FeinfocusDir	Varian Paxscan	1201	1 mm Al + 0.3 mm Cu	130	154	1200	82
Field samples T	FeinfocusDir	Varian Paxscan	1201	1 mm Al + 0.3 mm Cu	130	385	550	40
DH2	FeinfocusTra	Varian Paxscan	1201	1 mm Al + 0.3 mm Cu	130	385	550	43
DH4	FeinfocusDir	Varian Paxscan	1201	1 mm Al + 0.3 mm Cu	130	385	550	41
High resolution								
4 µm resolution	FeinfocusTra	Varian Paxscan	2001	1 mm Al	120	25	1500	113
2.8 µm resolution	FeinfocusTra	Varian Paxscan	2001	1 mm Al	100	30	2000	76

is determined for each individual object, so that a number of measurements are carried out per fracture to determine the aperture. The length of a fracture is determined by the diameter of the circumscribed sphere around the fracture. Additionally, stereographic projections of the orientation of the fractures were made. Because only a vertical orientation is known in the cores, the stereographic projections are most valuable in order to define a trend concerning the dip of the fractures.

Modelling

Based upon the 3D images analysed in Morpho+, a numerical model can be made of the rocks with the program 'E-core' developed by Lithicon, Norway (www.lithicon.com). Starting from the existing 3D image, in which the porosity is labelled as such, the pore network can be extracted. Subsequently, the network is simplified to a ball-and-stick model, or pore network model (PNM) (Bakke & Øren, 1997). It allows determining the maximum inscribed radius in pore bodies for volume calculations; the minimum inscribed radius in the pore throats for drainage capillary pressure and hydraulic conductance; and the pore shapes for describing the simultaneous flow of two or more fluids in one pore. This PNM is subsequently used as a basis for the computation of rock and fluid-flow properties. With multiphase fluid-flow simulations, one can determine the relative permeability of the rock for a specific fluid type. The simulations start with the model in which the pores are filled with water. After this there is a primary drainage with a non-wetting fluid. As a standard in E-core this is oil, but the properties of the fluid can easily be adjusted to those of liquid CO_2, with a density adaptable to the injection depth, pressure and temperature. For this study, the density of liquid CO_2 was set at 900 kg m^{-3}. E-core then gives a visual and statistical representation of the amount of pores which are now filled with water, trapped during the primary drainage, and the non-wetting fluid

representing liquid CO_2. What follows is a secondary drainage, filling the open porosity again with water. Now a statistical and visual representation is given of the pores filled with water trapped during the primary drainage, trapped CO_2 and water filling the pores after the secondary drainage.

Other properties, such as the absolute permeability of the rock samples can be determined by numerically solving differential equations directly on the virtual rock. For these simulations, a lattice Boltzmann (LB) method (Ramstad et al., 2010) is used to characterise the fluid flow. Detailed descriptions of the LB method and different lattices can be found in Chen & Doolen (1998) and Succi (2001). The model is known to closely mimic typical experimental set-ups (Ramstad et al., 2010). Therefore, this kind of analysis was carried out on selected samples in order to compare the results with experimentally determined permeability values of the rocks.

Results

Porosity and permeability in laboratory

Table 2 provides an overview of porosity values measured via the Archimedes method with water saturation (ϕ, vol.%) and those via He-porosimetry. Also, gas permeability measurements and the corresponding absolute, or empirical Klinkenberg permeability values are listed. Both porosity and permeability values are compared to values listed in Braathen et al. (2010, 2012) of rock samples in close proximity to the samples investigated in this research.

The open porosity of the samples ranges from as low as 1.05 to 13.86 vol.%. These results are all lower than the average porosity of 14% for the potential storage layers in the Knorringfjellet Formation described in the summary

Table 2. *Overview of porosity and permeability measurements carried out for this study, with a comparison to values from Braathen et al. (2010) of measurements carried out close to where the samples were taken*

From (m)	To (m)	Sample	Core	ϕ (vol%)	He-Poro. (vol.%)	Braathen et al. (2010) (vol.%)	Gas Perm. (mD)	Emp. Klink. Perm. (mD)	Braathen et al. (2010) (mD)
-671.92	-672.00	C9	Dh4	1.24	/	/	/	/	/
-674.48	-674.56	C8	Dh4	7.09	10.9	14.73	0.23	0.14	0.11
-677.12	-677.20	C7	Dh4	12.96	15.3	16.48	1.11	0.77	0.89
-680.94	-681.00	C6	Dh4	7.54	/	8.73	/	/	0.07
-687.10	-687.12	C5	Dh4	13.86	/	8.95	/	/	/
-689.64	-689.70	C4	Dh4	1.81	/	/	/	/	/
-691.00	-691.08	C3	Dh4	3.92	7.1	/	0.05	0.03	/
-693.96	-694.00	C2	Dh4	10.71	/	19.62	/	/	0.54
-695.22	-695.28	C1	Dh4	12.58	12.6	16.54	0.18	0.11	0.14
-736.73	-736.81	D1	Dh2	1.83	/	/	/	/	/
-741.67	-741.72	D2	Dh2	1.05	/	/	/	/	/
-752.30	-752.38	D3	Dh2	4.71	/	/	/	/	/

of the CO_2 project. Within this summary, porosity was determined through He-porosimetry and brine saturation (Braathen et al., 2010, 2012; Farokhpoor et al., 2010). When one compares porosity values calculated with water or brine saturation and by He-porosimetry, the results obtained with He-porosimetry are systematically higher than those calculated by water or brine saturation. This is because helium, a gas, can penetrate more open pores compared to water or brine.

MIP was used for the analysis of the porosity distributions in samples C4, C6, C7 and D3. The results

of these tests are shown in Fig. 4. In all samples except C7, the peak in pore diameter is found below 1000 nm (Fig. 4A). However, also in C7 the average pore diameter is far below 1 µm (102.6 nm). It is clear that the pores penetrated by mercury in the tested samples can best be described as nanopores. Presented in Table 3 are the pore characteristics per sample as determined from the MIP tests. In this table, the percentages are expressed as pore volumes and thus compared to the bulk rock volume. Together with Fig. 4A, it shows that from the four samples, C4 has the smallest pores, with 64.5% of its total pore volume penetrated by mercury found as pores
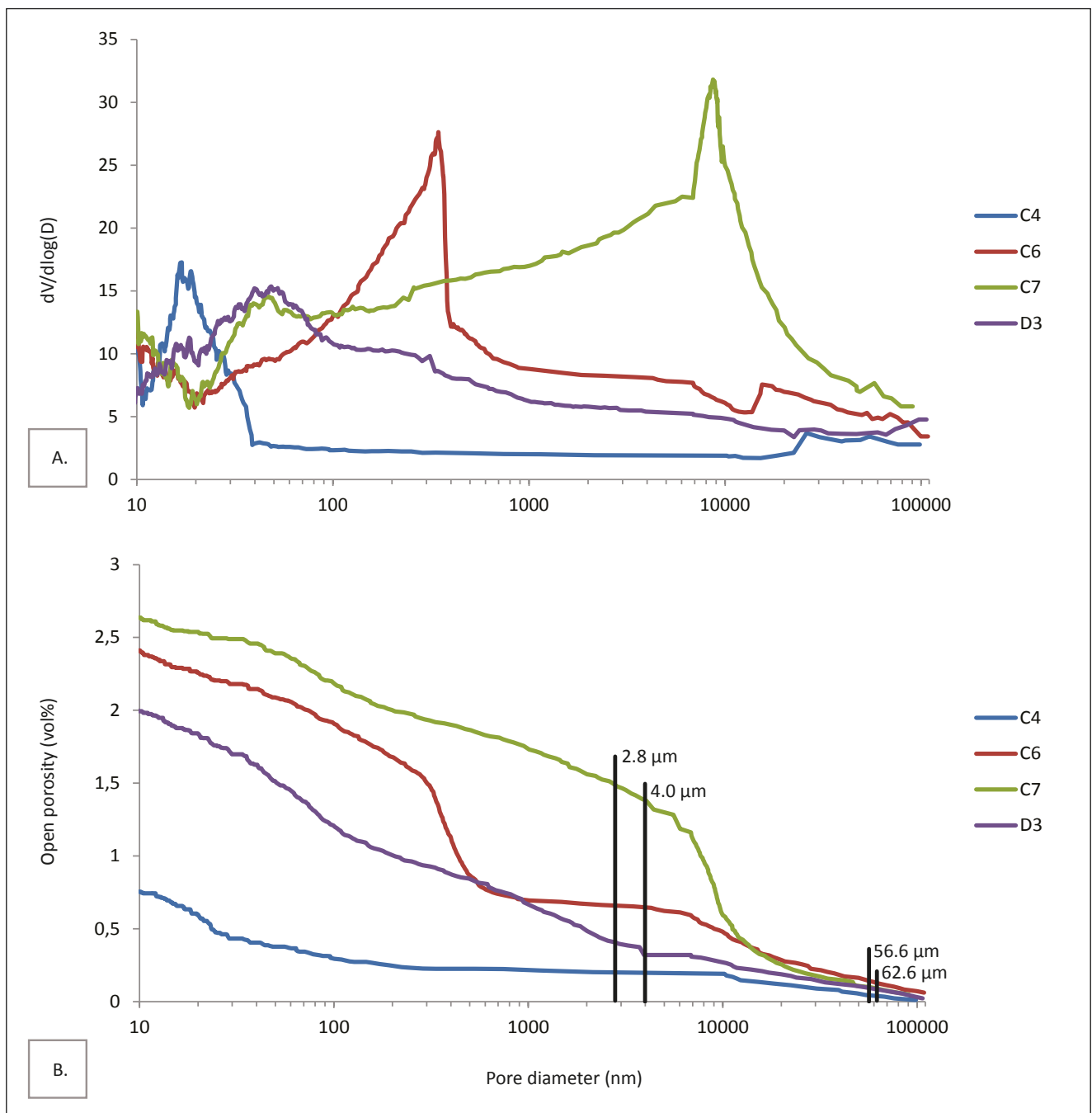

Figure 4. *Mercury Intrusion Porosimetry data of samples C4, C6, C7 and D3. (A) represents the pore size distribution from 10 nm to 100 µm expressed as the increase in pore volume in relation to the normal logarithm of the diameter. (B) represents the cumulative curve in which the porosity of the tested sample is expressed relative to the pore diameter.*

Table 3. *Overview of the results from the Mercury Intrusion Porosimetry tests for samples C4, C6, C7 and D3.*

Sample #	Average pore diameter (nm)	(%) pore volume smaller than 100 nm	(%) pore volume smaller than 500 nm	(%) pore volume smaller than 1 μm	(%) pore volume smaller than 2.8 μm	(%) pore volume smaller than 4 μm	(%) pore volume smaller than low resolution scan
C4	26.1	0.55	0.62	0.63	0.65	0.65	0.80
C6	69.6	0.59	1.63	1.81	1.85	1.99	2.37
C7	102.6	0.52	0.84	0.96	1.21	1.32	2.60
D3	58.2	0.84	1.20	1.38	1.63	1.73	1.96

with a diameter smaller than 100 nm. In this sample, only a small range of pore sizes is present (Fig. 4A). The peak of pore diameter in sample C6 (Fig. 4A) lies between 100 and 500 nm. The spreading of the peak indicates a broad range of pore sizes present in the sample. A similar observation is made for sample C7 and sample D3. Fig. 4B displays the cumulative distribution of the pore sizes compared to the volume penetrated by mercury. In this figure, the resolutions at which the scans are taken are indicated.

CT-analysis

In Table 4, the results of the scans with regard to the segmented porosity are presented. For each sample, the observed porosity is given at the resolutions at which the sample was scanned. For example, sample C7 showed a porosity of 3.07 vol.% at scans with a resolution of 56.61 μm. When scanned at a higher resolution (4 μm), pores smaller than 56.61 μm could also be visualised, leading to a total observed porosity of 10.11 vol.%. HRXCT made it possible to visualise a porosity higher than 0 vol.% in all scanned core samples taken from Dh2 and Dh4 except for sample C9. This sample was taken from the cap-rock sequence in Dh4 and was only scanned at a resolution of 56.61 μm. In only five of the 10 scanned field samples could pores be determined. These were T1, T3, S2, S6

and S7. Other samples were only analysed at the lowest resolution of 41 μm (T4, T5, S3, and S8) or did not show porosity at scans with a resolution of 4 μm.

The results listed in Table 4 give an idea of the pore-size distributions within the samples. Since even at the highest resolutions (4, 2.8 and 1.68 μm) obtained, the pore space which could be visualised is still below the porosity as measured with water saturation for all samples, so pores must be present which are smaller than these resolutions. In Fig. 5, several slices through the scans are given as an example of how the pore space is visualised. This figure shows the samples with the highest porosities. In both the field samples and the samples from Dh2 and Dh4, these are the conglomerates from the Brentskardhaugen Bed (C7 and S6) in which one can extract a similar porosity of approximately 10.5 vol.%. However, in Fig. 5A, B, which represents field sample S6, the pore space is visualised at a resolution of 41 μm while in Fig. 5C, D, representing sample C7 from Dh4, the pore space could only be represented to its full extent at a higher resolution of 4 μm. In some samples, such as C1 and C5 which are characterised by porosities higher than 10 vol.%, one is still not capable of visualising the major part of the pore space despite a resolution of 4 μm. This deficiency is even more pronounced in the high-resolution scans of the field samples. Results from the

Table 4. *Overview of the observed porosity in scans carried out at different resolutions of both core samples and field samples.*

Dh4 & Dh2	ϕ>56.61 μm (vol.%)	ϕ>4 μm (vol.%)	ϕ>2,8 μm (vol.%)	ϕ>1,68 μm (vol.%)	Lab poro. (vol.%)	Field samples	ϕ>41 μm (vol.%)	ϕ>4 μm (vol.%)	Lab poro. (vol.%)
C9	0.00	-	-	-	1.24	T5	0.00	-	5.78
C8	0.02	-	-	-	7.09	S8	0.00	-	12.09
C7	3.07	10.11	-	-	12.96	S7	0.94	3.68	4.47
C6	0.00	-	6.86	-	7.54	S6	10.85	-	16.76
C5	-	0.22	-	-	13.86	S3	0.00	-	5.96
C4	0.05	-	0.59	-	1.81	S2	-	0.68	7.85
C3	0.00	2.90	-	-	3.92	T4	0.00	-	7.00
C2	1.93	-	-	-	10.71	T2	0.00	0.00	5.13
C1	5.76	4.48	-	-	12.58	T3	0.00	0.90	9.03
D1	0.00	0.96	-	-	1.83	T1	0.00	2.56	9.68
D2	0.20	-	-	0.83	1.05				
D3	2.06	2.25	2.45	-	4.71				

Mercury Intrusion Porosimetry tests are therefore used for a full description of the pore-size distribution. These tests were carried out on samples C4, C6, C7 and D3 and the results are presented in Table 3 and Fig. 4.

Fractures in the samples were characterised for their maximum aperture and length as well as for their orientation inside the sample. These calculations were carried out on both the field samples and the core samples, which were characterised by the presence of fractures. One of the most striking differences between the field samples and the core samples is the difference

in fracture distribution; in all nine samples from the field, which were scanned at low resolution (41 μm), fractures were observed, while in the scans with the lowest resolution (56.61 μm) taken from the core samples, only four of the 11 samples which were scanned showed the occurrence of fractures (C1, C3, C4 and C8). D2, a sample taken from Dh2, showed the occurrence of veins with mineral infill. At a resolution of 4 and 2.8 μm, respectively, samples C3 and C4 show the occurrence of small fractures. From the scans it is clear that the fractures are commonly related to a competence contrast between different layers. This can be seen by the fact
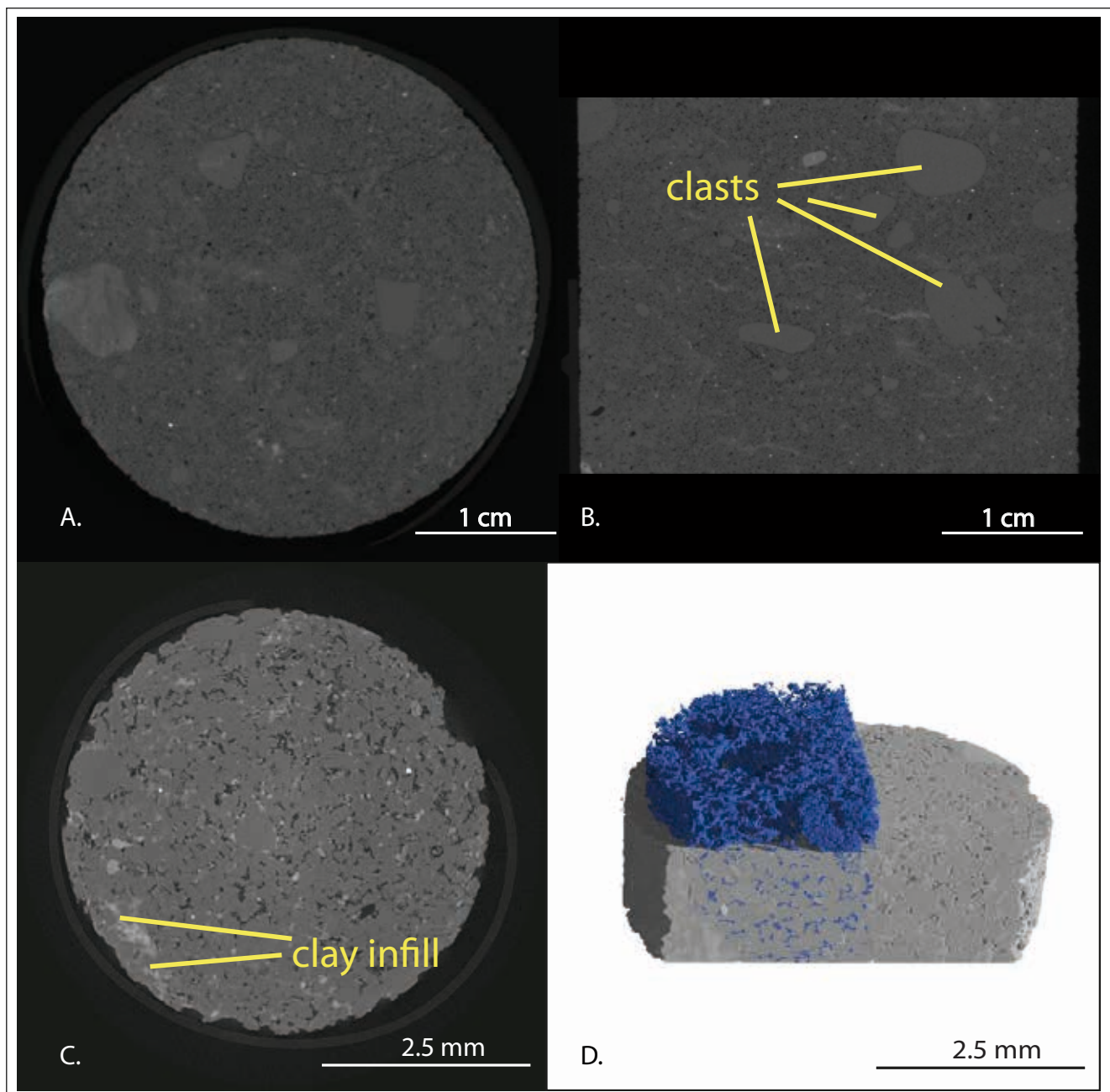

Figure 5. *Cross-sections through scans of samples S6 (A) and (B), and C7 (C) and (D), in order to illustrate the porosity as seen on scans. (D) represents a 3D volume of sample C7 at a resolution of 4 μm in which the pores are extracted and visualised in blue. One can also distinguish pores which are filled with clay minerals. (A) and (B) have a resolution of 41 μm. In these images, individual clasts can be recognised as well as the porosity of the rock sample. (C) and (D) have a resolution of 4 μm in which pores can be recognised as well as clay minerals which partly fill up the porosity.*

that they commonly follow borders between sandstone lithologies and clay layers. This is an observation that has also been made by Ogata et al. (2012, 2014). As an example, images are given from sample C4 from Dh4 in Fig. 6. In this sample, fractures were observed at a resolution of 56.61 µm and at a higher resolution of 2.8 µm. The sample matrix is characterised by a significant amount of clay in which pyrite concentrations are found as pyrite chambers which are interlinked by a network of pyrite tubes. This chamber and channel configuration reflects a fossilised burrow system belonging to the ichnogenus *Thalassinoides*. The burrow system resembles that of recent mud shrimp species such as *Upogebia* affinis, described by Bromley & Frey (1974). Some of the fractures in the sample seem to be linked to this pyrite structure. In Fig. 6A, which shows the sample at a resolution of 56.61 µm, the fractures are encircled and one can see the structure of pyrite chambers and tubes as bright spots. In Fig. 6B, the sample is visualised at a higher resolution of 2.8 µm. At this resolution, even smaller fractures could be visualised. Fig. 6C, D gives a 3D representation of the rock in both low and high resolution. At low resolution the pyrite network is visible, as well as fractures, while at high resolution only one small fracture can be distinguished.

Fig. 7A gives an overview of the fracture apertures in samples in which fractures could be segmented with the MSHFF script. It concerns six field samples (T1 to T5 and S3) and three core samples (C3, C4 and C8) from Dh4.
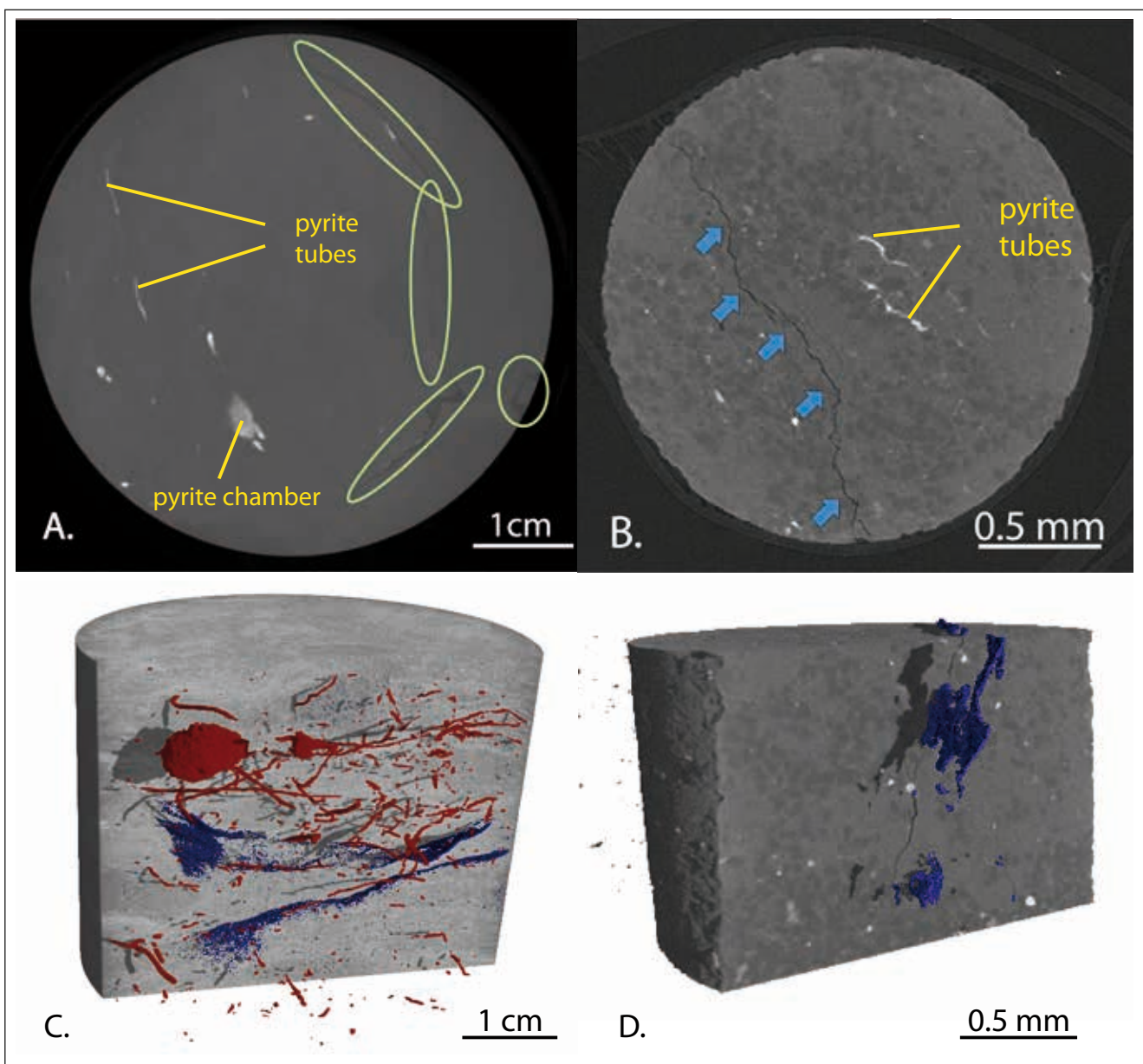

Figure 6. Cross-sections through scans of sample C4 at a resolution of 56.6 µm (A), and 2.8 µm (B). In these cross-sections fractures are indicated and the network of pyrite tubes and chambers can be seen as bright spots. This reflects the trace fossil burrow system ascribed to the ichnogenus Thalassinoides. In figures (C) and (D), a 3D rendering is given of the sample at resolutions of 56.6 and 2.8 µm, respectively. The pyrite network is indicated in red and fractures in blue.
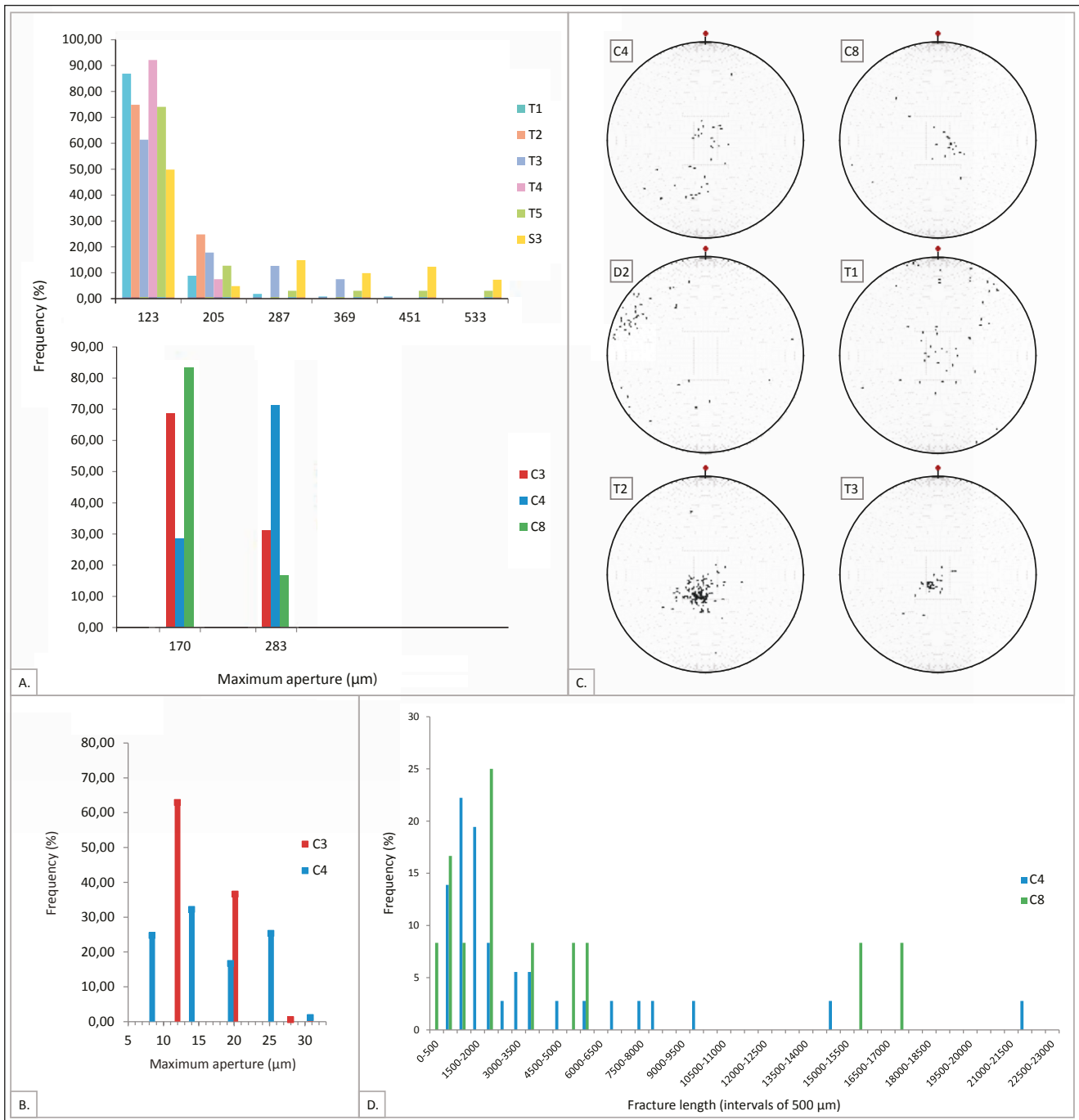
Figure 7. Overview of the obtained results concerning fractures measured in field samples (S- and T-samples) and core samples (C-samples). (A) shows the distribution of the maximum openings of the fractures observed at low resolution (41 μm for the field samples and 56.6 μm for the core samples); (B) illustrates the maximum opening of small fractures observed in samples C3 and C4 at resolutions of 4 and 2.8 μm, respectively; (C) shows stereographic projections of fractures in samples C4, C8, D2, T1, T2 and T3. All stereographic projections are based on fracture analysis at low resolution. Samples C4, C8, T2 and T3 show a distinct horizontal orientation of the fractures, D2 shows a vertical orientation and T1 is characterised by a dual trend; both horizontal and vertical. (D) illustrates the distribution of fracture lengths in samples C4 and C8 scanned at a resolution of 56.6 μm.

These measurements are the result of scans with low resolution (41 μm for the field samples and 56.61 μm for the core samples) and they allow us to compare fracture apertures in the field with those in the core samples. In two subsamples, C3 and C4, small fractures were observed. Fig. 7B is a histogram depicting the maximum apertures in them. The orientation of the fractures is described by stereographic projections as illustrated in Fig. 7C. Here, six stereographs depict mainly horizontal fractures in samples C4, C8, T2 and T3, vertical fractures in sample D2 and randomly orientated fractures in sample T1. Overall, the samples show a dual trend concerning the distribution of fracture orientations in which most fractures are horizontally orientated, while some other fractures show an inclined, or even vertical orientation. In some samples, this distinction is less clear.

There, fractures seem to follow clay-rich layers of the rock and are distributed within them. A last parameter to describe fractures is their length, given in Fig. 7D. There the distribution of lengths for different fractures observed in samples C4 and C8 in Dh4 at a resolution of 56.6 μm is presented.

Modelling

Rock modelling was carried out on four samples: C1, C3, C6 and C7. The basis for the modelling were scans of core samples at resolutions of 4 and 2.8 μm in which only conventional pores were included. Fractures were thus not considered in the models. The first step in this process was the extraction and simplification of the pore network from the rocks. It allowed the pores to be characterised according to their shape and size. In all samples, E-core calibrated the majority of the pores to have triangular shapes. Also, their average pore radius is similar in all samples, ranging between 6.5 and 11.8 μm. The networks of samples C1 and C3 were considered to be too tight for fluid-flow simulations. Therefore, flow simulations were only carried out on samples C6 and C7. These samples had a total porosity of 7.2 vol.% and 10.4 vol.%, respectively. In Table 5, an overview is given of the CO_2 trapped in the system after each consecutive step of the fluid-flow simulation: a primary drainage with CO_2, a water-flooding stage and a secondary drainage with CO_2. Although it is known that in both C6 and C7 a certain amount of pores remains undetected in the scans due to the resolution, these simulations can be considered to be close to reality, since it is known that the non-wetting fluid (in this case liquid CO_2) flows through the biggest pores (Blunt, 2001).

In the flow simulation through sample C6, the CO_2 did not enter the pores in one smooth flow. With increasing pressure, several jumps in CO_2 saturation could be observed. This indicates that the threshold porosity lacks effective connections between the pores. From the MIP data it is known that there are a significant number of pores smaller than the resolution obtained with CT (2.8 μm), so that scanning at a higher resolution would increase the connectivity between pores. Also, when one compares the permeability obtained during the simulation of samples C6 and C7 to the known permeability from laboratory measurements (reference permeability in Table 5), it is clear that the values of 0.43 and 11 mD are too high. In this analysis, the permeability of C6 is compared to measurements by Braathen et al. (2010), while the permeability of C7 is compared to permeability measurements carried out specifically for this study.

Discussion

Porosity and permeability in laboratory

For the core samples from Dh2 and Dh4, the values for open porosity are found between 1.05 and 13.86 vol.%. These are relatively low values compared to the expected values from previous studies, as described by Braathen et al. (2012). Also, values for open porosity from the field samples are found within this range, with the exception of a conglomerate sample from the Brentskardhaugen Bed which reached an open porosity of 16.76 vol.%. It was taken from a lens within this Bed which was low in iron as compared to the surrounding rocks. Results from He-porosimetry, however, suggest that for some samples the actual open porosity might be higher than what was measured with water saturation. This is in accordance with the fact that the water absorption detects only open pores larger than 100 nm (Cnudde et al., 2009). From the four samples in which the porosity was additionally determined by He-porosity, three samples showed a significantly higher porosity with this second technique. In these samples the measured porosity was up to 3.81 vol.% higher than the values obtained with water saturation. This indicates that part of the pore space is represented by pores smaller than this detection limit. The analysis of samples C4, C6, C7 and D3 with MIP shows the nanoporous nature of the rocks. Average pore diameters range from 26.1 nm (C4) to 102.6 nm (C7). However, the upper detection limit of the MIP method is about 60 μm (Cnudde et al., 2009), so larger pores are not withheld in this technique.

Permeability values show a great correspondence with the earlier results from Braathen et al. (2012). All samples show a permeability lower than 1 mD, with the highest permeability measured in a conglomerate sample of the Brentskardhaugen Bed. These values, combined with borehole water injection tests, thus suggest that fractures enhance the lateral fluid flow.

CT-analysis

When one compares the results of the laboratory measurements of open porosity with the results obtained

Table 5. *Intrusion of liquid CO_2 into the pore network of samples C6 and C7 after different stages of the fluid-flow simulation.*

	After primary drainage with CO_2	After waterflooding with CO_2	After secondary drainage with CO_2	Permeability (mD)	Reference permeability (mD)
C6	61%	50%	61%	0.43	0.07
C7	87%	59%	87%	11	0.77

with CT analysis, the pore space present in the CT images does not represent the total pore network. Based only on the segmentation of pores in these images, the porosity would systematically be estimated too low. The segmentation of pores suggests the presence of pores smaller than the resolution in all scanned samples. Taking sample C3 as an example, via He-porosity it is known that there are a significant number of micro-pores. With this technique an open porosity of 7.1 vol.% is obtained. However, in CT scans at a resolution of 4 μm the pores only represent 2.9% of the sample, indicating that a significant amount of the pores remains undetected in these images. A detailed analysis of the distribution of pore sizes within a sample is given when it is subjected to MIP. These tests have shown the nanoporous nature of the samples. When the segmented pore space is exported to E-Core, the pores can be further analysed. After the simplification of this network, an average pore radius of 8.5 μm was obtained in a selection of over 26,000 pores. The maximum pore radius was 36.5 μm. Similar observations can be made in other samples, suggesting an important contribution of small pores (<4 μm) in the analysed sandstone sections. Analysis of these pores thus requires a higher resolution of scanning, but in order to obtain a resolution of 1 μm, subsamples with a maximum diameter of 1 to 2 mm should be scanned. The question then remains to what extent subsamples this small are representative for larger scales.

Fracture analysis was an important part of the research. In order to characterise fractures in 3D, three main parameters were determined for the fractures: their aperture, length and orientation. Also, the fractures were compared between field samples and core samples. An important difference between fractures found in field samples and those in core samples is found in their overall presence. Fractures were found in all field samples, whereas they were present in only six out of eleven scanned core samples. This difference can be explained by the model of Ogata et al. (2012) in which decompaction, because of unroofing, leads to reworking of pre-existing fractures. Also, crack propagation by frost wedging is a possible mechanism through which these differences can be explained, since the fractures are characterised by a geometry which is prone to propagation under the stress of freeze-thaw cycles (Tharp, 1987). The same mechanisms can be applied to explain the difference in fracture length between outcrop fractures and those found in the cores. Generally, the fractures in the field samples are found throughout the entire diameter of the cylindrical samples and must thus be considered as a minimum length, whereas the length of fractures is limited in core samples to a maximum of 2.1 cm. If the reservoir underpressure is considered, the fractures are thought to be prone to open when subjected to relatively small pressure increments (Ogata et al., 2012). Fracture apertures are similar in both field samples and core samples which is in accordance with the model proposed by Ogata et al. (2012). Although there are some outliers

in which fractures in field samples are found to have an aperture of up to 0.5 mm, most apertures range between 123 and 283 μm. Fractures observed at high resolution (4 and 2.8 μm) are characterised by apertures of only 25 μm. Fractures have a predominant horizontal orientation in both field samples and core samples. However, in some samples there is also a significant amount of fractures with either a vertical or an inclined orientation. Also, the small fractures observed in two samples scanned at high resolution have a primary horizontal orientation, with an additional vertical component in some of these fractures. The observation of primarily horizontal fractures, which are sometimes interconnected via vertical fractures, can be explained by the fact that the fractures at this scale are most commonly related to the competence contrast between different layers. They follow boundaries between sandstone sections and the interbedded clay. The predominant horizontal orientation of fractures seems to be in disagreement with the observations of Ogata et al. (2012); they suggested that coarser-grained sandstone intervals enhance vertical communication between different layers because of a general vertical orientation of fractures in these intervals. It is, however, just a question of scale: the observations of Ogata et al. (2012) are made at a mesoscopic level, while for this study the focus was on the study of the rocks on a pore-scale. At this level, fractures found in sandstone layers are predominantly horizontally orientated.

Modelling

Four samples were selected for rock modelling since they were scanned at a highest obtained resolution: C1, C3 and C7 obtained a resolution of 4 μm and C6 was characterised with a resolution of 2.8 μm. The pore network was extracted and simplified to a ball-and-stick model from which quantitative data of the pores could be extracted. Although some pores smaller than the resolution remained undetected, the analysis is still valid since the non-wetting fluids of interest will flow preferentially through the biggest pores. The analysis of the pore network revealed that the average pore radius in these samples is found between 6.5 and 11.8 μm. Considering that on the scans which formed the basis for the modelling step, not the entire pore space was visualised and thus pores smaller than the resolution should only be considered, these values are low. Even when the largest pores are considered, the radii only go up to 72.4 μm. In two samples, C1 and C3, the pore connectivity was too weak to perform fluid-flow simulations. Therefore, they were only carried out in samples C6 and C7. In these samples an effective uptake of liquid CO_2 was established at 61% and 87%, respectively, after primary drainage of the pore network. Subsequent water flooding lowers these levels to 50% and 59%. These simulations are encouraging for potential CO_2 storage; however, upon closer inspection of the permeability calculated in the simulations one notices these are higher than the actual values. A first reason for

this difference is that the experimental measurements and the simulations were not carried out on exactly the same rock volume. Within the heterogeneous matrix of the rock, this will therefore bias the results. Another source of uncertainty lies within the assignment of hydraulic conductance to pore bodies and throats in the simulations (Bakke & Øren, 1997).

Conclusions

Using HRXCT, sandstone and conglomerate intervals of the Knorringfjellet Formation were analysed with a resolution up to 2.8 μm. In spite of this resolution, the pore network was not visualised totally. However, porosity measurements at different scanning resolutions and from laboratory measurements with water saturation and He-porosimetry did show a pore-size distribution in which small pores seem to be abundantly present. These small pores are partially responsible for the low permeability in the rocks. Although it remains difficult to compare the water saturation method with results from micro-CT and MIP, due to the different approaches and physical basis of the tests, the combined results give a better insight into the pore-size distribution within the rocks (Cnudde et al., 2009). Also, for the first time since the start of the Longyearbyen CO_2 Lab project, hard data were presented on the fracture aperture distribution within the Knorringfjellet Formation. This is a critical parameter for the simulation of the natural fracture network. Fracture apertures in both the field section and the core sections of the Knorringfjellet Formation range from 41 to 533 μm; however, the majority of the fractures is characterised by an aperture between 123 and 283 μm. Some smaller fractures, which were observed only in sandstone samples from cores Dh2 and Dh4, were characterised by apertures of 8 to 25 μm. Also, other fracture parameters were determined for the first time at a pore scale, such as their orientation, occurrence and length. Although the fractures have a distinct primary horizontal orientation, a significant number of the fractures are characterised by a vertical orientation. They occur at boundaries between different lithologies. When found in outcrop, fractures tend to be longer and more pronounced as opposed to fractures found in the cores. This fits with the model proposed by Ogata et al. (2012) in which decompaction because of unroofing leads to reworking of pre-existing fractures, as well as with the theory of crack propagation due to frost wedging. HRXCT thus allowed a detailed analysis of fractures in both field samples and core samples at a pore scale. Together with the analysis of the pore network, simulations could be carried out, visualising the multi-phase flow of liquid CO_2 through an original water-saturated pore network. Although pores smaller than the resolution were not taken into account during these simulations, the pore network was considered to be accurate enough to approach the actual permeability of the sample to approximately ten times the actual permeability. These simulations thus partially visualised the uptake of CO_2 at a pore scale.

In order to obtain a more detailed understanding of the influence of the observed fractures on the uptake and flow of CO_2 in the reservoir, further studies are necessary. In these studies the precise distributions of different phases within the fractures need to be characterised and the communication between the flow in the pores and fractures needs to be analysed.

References

Bäckström, S.A. & Nagy, J. 1985: Depositional history and fauna of a Jurassic phosphorite conglomerate (the Brentskardhaugen Bed) in Spitsbergen. *Norsk Polarinstitutt Skrifter 183*, 1–61.

Bakke, S. & Øren, P.E. 1997: 3-D Pore-Scale Modelling of Sandstones and Flow Simulations in the Pore Networks. *Society of Petroleum Engineers Journal 2*, 136–149.

Berkowitz, B. 2002: Characterizing flow and transport in fractured geological media: a review. *Advances in Water Resources 25*, 861–884.

Blunt, M.J. 2001: Flow in porous media – pore-network models and multiphase flow. *Current opinion in colloid & interface science 6*, 197–207.

Braathen, A., Bælum, K., Christiansen, H., Dahl, T., Flå, H., Hansen, F., Hanssen, T.H., Jochmann, M., Johansen, T.A., Mertes, J., Mørk, A., Nemec, W., Olaussen, S., Sand, G. & Tveranger, J. 2010: Longyearbyen CO_2 Lab 2007-2009 – Phase 1. Final Report. *University Centre of Svalbard (UNIS) Report, 2010 – 2012*, Longyearbyen, 69 pp.

Braathen, A., Bælum, K., Christiansen, H.H., Dahl, T., Eiken, O., Elvebakk, H., Hansen, F., Hanssen, T.H., Jochmann, M., Johansen, T.A., Johnsen, H., Larsen, L., Lie, T., Mertes, J., Mørk, A., Mørk, M.B., Nemec, W., Olaussen, S., Oye, V., Rød, K., Titlestad, G.O., Tveranger, J. & Vagle, K. :2012: The Longyearbyen CO_2 Lab of Svalbard, Norway – initial assessment of the geological conditions for CO_2 sequestration. *Norwegian Journal of Geology 92*, 353–376.

Brabant, L., Vlassenbroeck, J., De Witte, Y., Cnudde, V., Boone, M.N., Dewanckele, J. & Van Hoorebeke, L. 2011: Three-dimensional analysis of high-resolution X-ray computed tomography data with Morpho+. *Microscopy and Microanalysis 17*, 252–263.

Bromley, R.G. & Frey, R.W. 1974: Redescription of the trace fossil Gyro-lithes and taxonomic evaluation of Thalassinoides, Ophiomorpha and Spongeliomorpha. *Bulletin of the Geological Society of Denmark 23*, 311–335.

Chen, S. & Doolen, G.D. 1998: Lattice Boltzmann Method for Fluid Flows. *Annual review of Fluid Mechanics 30*, 329–364.

Cnudde, V. & Boone, M.N. 2013: High-resolution X-ray computed tomography in geosciences: A review of the current technology and applications. *Earth-Science Reviews 123*, 1–17.

Cnudde, V., Cwirzen, A., Masschaele, B. & Jacobs, P.J.S. 2009: Porosity and microstructure characterization of building stones and concretes. *Engineering geology 103*, 78–83.

Farokhpoor, R., Torsæter, O., Baghbanbashi, T., Mørk, A. & Lindeberg, E.G.B. 2010: Experimental and Numerical Simulation of CO_2 Injection into Upper-Triassic Sandstones in Svalbard, Norway. *Abstracts and Proceedings, Society of Petroleum Engineers International Conference on CO_2 Capture, Storage, and Utilization, 10–12 November, New Orleans, Louisiana, USA*, SPE 139524.

Farokhpoor, R., Baghbanbashi, T., Torsæter, O., Lindeberg, E. & Mørk, A. 2011: Experimental and Simulation Analysis of CO_2 Storage in Tight and Fractured Sandstone under Different Stress Conditions. *Abstracts and Proceedings, Society of Petroleum Engineers Annual Conference and Exhibition, 23–26 May, Vienna, Austria*, SPE 143589.

León, C.A.L. 1998: New perspectives in mercury porosimetry. *Advances in Colloid and Interface Science 76–77*, 341–372.

Masschaele, B.C., Cnudde, V., Dierick, M., Jacobs, P., Van Hoorebeke, L. & Vlassenbroeck, J. 2007: UGCT: New X-ray radiography and tomography facility. *Nuclear Instruments and Methods in Physics Research Section A: Accelerators, Spectrometers, Detectors and Associated Equipment 580*, 266–269.

Mørk, A., Dallmann, W.K., Dypvik, H., Johannessen, E.P., Larssen, G.B., Nagy, J., Nøttvedt, A., Olaussen, S., Pchelina, T.M. & Worsley, D. 1999: Mesozoic lithostratigraphy. *In* Dallmann, W.K. (ed.): *Lithostratigraphic Lexicon of Svalbard*, Norsk Polarinstitutt, Tromsø, pp. 127–214.

Mørk, M.B.E. 2013: Diagenesis and quartz cement distribution of low-permeability Upper Triassic-Middle Jurassic reservoir sandstones, Longyearbyen CO_2 Lab well site in Svalbard, Norway. *American Association of Petroleum Geologists Bulletin 97*, doi:10.1306/10031211193.

Nagy, J. & Berge, S.H. 2008: Micropalaeontological evidence of brackish water conditions during deposition of the Knorringfjellet Formation, Late Triassic-Early Jurassic, Spitsbergen. *Polar Research 27*, 413–427.

NBN EN 1936:2006. Natural stone test methods – Determination of real density and apparent density and of total and open porosity. CEN, Brussels.

Ogata, K., Senger, K., Braathen, A., Tveranger, J. & Olaussen, S. 2012: The importance of natural fractures in a tight reservoir for potential CO_2 storage: a case study of the upper Triassic–middle Jurassic Kapp Toscana Group (Spitsbergen, Arctic Norway). *In* Spence, G.H., Redfern, J., Aguilera, R., Bevan, T.G., Cosgrove, J.W., Couples, G.D. & Daniel, J.-M. (eds.): *Advances in the Study of Fractured Reservoirs*, Geological Society of London Special Publication 374, PAGES, doi: 10.1144/sp374.9.

Ogata, K., Senger, K., Braathen, A., Tveranger, J. & Olaussen, S. (2014): Fracture systems and meso-scale structural patterns in the siliciclastic Mesozoic reservoir-caprock succession of the Longyearbyen CO_2 Lab project: implications for geologic CO_2 sequestration on Central Spitsbergen, Svalbard. *Norwegian Journal of Geology 94*, 121–154.

Ramstad, T., Øren, P.-E. & Bakke S. 2010: Simulation of Two-phase flow in Reservoir Rocks Using a Lattice Boltzmann Method. *Society for Petroleum Engineers Journal*, SPE 124617.

Riepe, L., Suhaimi, M.H., Kumar, M. & Knackstedt, M.A. 2011: Application of high resolution micro-CT-imaging and Pore Network Modeling (PNM) for the petrophysical characterization of tight gas reservoirs – A case history from a deep clastic tight gas reservoir in Oman. *Society of Petroleum Engineers Middle East Unconventional Gas Conference and Exhibition, 31 January – 2 February, Muscat, Oman*, SPE-142472-PP.

Succi, S. 2001: *The Lattice Boltzmann Equation for Fluid Dynamics and Beyond*. Oxford University Press, 304 pp.

Tharp, T.M. 1987: Conditions for crack propagation by frost wedging. *Geological society of America Bulletin 99*, 94–102.

Throndsen, T. 1982: Vitrinite reflectance studies of coals and dispersed organic matter in Tertiary deposits in the Adventdalen area, Svalbard. *Polar Research 1982*, 77–91.

Vlassenbroeck, J., Dierick, M., Masschaele, B., Cnudde, V., Van Hoorebeke, J. & Jacobs, P. 2007: Software tools for quantification of X-ray microtomography at the UGCT. *Nuclear Instruments and Methods in Physics Research 580*, 442–445.

Voorn, M., Exner, U. & Rath, A. 2013: Multiscale Hessian fracture filtering for the enhancement and segmentation of narrow fractures in 3D image data. *Computers & Geosciences 57*, 44–53.

Wærum, G.O. 2011: *Fracture patterns in the Triassic De Geerdalen Formation – implications for migration of CO_2*. MSc thesis, University of Tromsø, 91 pp.